ADVANCED OPTICAL MATERIALS
www.advopticalmat.de

Reversible Single-Pulse Laser-Induced Phase Change of Sb_2S_3 Thin Films: Multi-Physics Modeling and Experimental Demonstrations

*Capucine Laprais, Clément Zrounba, Julien Bouvier, Nicholas Blanchard, Matthieu Bugnet, Alban Gassenq, Yael Gutiérrez, Saul Vazquez-Miranda, Shirly Espinoza, Peter Thiesen, Romain Bourrellier, Aziz Benamrouche, Nicolas Baboux, Guillaume Saint-Girons, Lotfi Berguiga, and Sébastien Cueff**

Phase change materials (PCMs) have gained a tremendous interest as a means to actively tune nanophotonic devices through the large optical modulation produced by their amorphous to crystalline reversible transition. Recently, materials such as Sb_2S_3 emerged as particularly promising low loss PCMs, with both large refractive index modulations and transparency in the visible and near-infrared. Controlling the local and reversible phase transition in this material is of major importance for future applications, and an appealing method to do so is to exploit pulsed lasers. Yet, the physics and limits involved in the optical switching of Sb_2S_3 are not yet well understood. Here, the reversible laser-induced phase transition of Sb_2S_3 is investigated, focusing specifically on the mechanisms that drive the optically induced amorphization, with multi-physics considerations including the optical and thermal properties of the PCM and its environment. The laser energy threshold for reversibly changing the phase of the PCM is determined through both theoretical analysis and experimental investigation, not only between fully amorphous and crystalline states but also between partially recrystallized states. Then, the non-negligible impact of the material's polycrystallinity and anisotropy on the power thresholds for optical switching is revealed. Finally, the challenges related to laser amorphization of thick Sb_2S_3 layers are addressed, as well as strategies to overcome them. These results enable a qualitative and quantitative understanding of the physics behind the optically-induced reversible change of phase in Sb_2S_3 layers.

1. Introduction

Recent advances in nanophotonics have opened up unprecedented opportunities for controlling light–matter interactions at the nanoscale. Yet, as of today, most devices are passive, and hence, limited to one dedicated functionality set at the fabrication stage. Implementing tunable and reconfigurable capabilities on devices appear now as a necessity to unlock the full potential of nanophotonics. For that matter, functional materials have recently gained attention for tunable nanophotonics as they can allow dynamic control of light without any moving parts.[1]

In this regard, phase change materials (PCMs) are highly promising, when integrated with waveguides and metasurfaces, for applications in telecommunications, displays, sensing or neural network.[2,3] Their particularity is the possibility to rapidly and reversibly change their state from amorphous to crystalline. This phase transition is non-volatile and induces a much larger change in refractive index than other tuning mechanisms.[4,5] Most of the works on PCMs focus on standard PCMs

C. Laprais, C. Zrounba, J. Bouvier, A. Benamrouche, N. Baboux, G. Saint-Girons, L. Berguiga, S. Cueff
CNRS, Ecole Centrale de Lyon, INSA Lyon
Universite Claude Bernard Lyon 1, CPE Lyon, INL, UMR5270
Ecully 69130, France
E-mail: sebastien.cueff@ec-lyon.fr

The ORCID identification number(s) for the author(s) of this article can be found under https://doi.org/10.1002/adom.202401214

© 2024 The Author(s). Advanced Optical Materials published by Wiley-VCH GmbH. This is an open access article under the terms of the Creative Commons Attribution License, which permits use, distribution and reproduction in any medium, provided the original work is properly cited.

DOI: 10.1002/adom.202401214

N. Blanchard, A. Gassenq
Universite Claude Bernard Lyon 1, CNRS
Institut Lumière Matière, UMR5306
Villeurbanne F-69100, France

M. Bugnet
CNRS, INSA Lyon
Universite Claude Bernard Lyon 1, MATEIS, UMR 5510
Villeurbanne 69621, France

Y. Gutiérrez
Departamento de Física Aplicada
Universidad de Cantabria
Avenida de los Castros, s/n, Santander 39005, Spain

S. Vazquez-Miranda, S. Espinoza
ELI Beamlines Facility
The Extreme Light Infrastructure ERIC
Za Radnicí 835, Dolní Břežany 25241, Czech Republic

 © 2024 The Author(s). Advanced Optical Materials published by Wiley-VCH GmbH

such as GST or GeTe, used as switches between the amorphous and crystalline state. Although these PCMs have been successfully used as memory elements on waveguides,[6] as artifical synapses and neurons,[7–9] for tunable absorbers,[10–12] beam steerers[13,14] or color filters,[15] they are often too lossy for specific applications in the visible and near infrared ranges.[16] For this reason, a new class of emerging PCMs, so-called "low loss PCMs," have been the subject of increasing interest. Sb_2S_3 is one of these PCMs, it has recently been introduced to the photonics community by Dong et al.[17] for its exciting optical properties: beyond 780 nm it presents a negligible absorption in both phases while its refractive index contrast remains very large ($\Delta n = 1$).[17–19] However, being an emerging PCM, Sb_2S_3 has not yet reached the maturity of GST, and many of its functional aspects need to be understood and optimized, especially its switching performances (e.g., switching time, cyclability).[16] Additionally, recent years have witnessed a paradigm shift toward prioritizing multi-level phase transition rather than using PCMs as simple binary switches. While controlling the partial recrystallization of unpatterned Sb_2S_3 thin films has been demonstrated,[20] only a few studies reported the control of the reversible partial phase transition at the device level.[21–23] Accordingly, developing approaches for locally controlling the phase transition of Sb_2S_3 is essential and demands a comprehensive understanding of the involved phenomena.

Among the possible methods for inducing the phase transition, the optical switch is very versatile as it allows a local and reversible phase change[24–26] without additional fabrication steps such as the integration of micro-heaters. The physical principle of the switch is straightforward: the laser energy absorbed within the PCM generates heat, which subsequently provokes the change of phase once the crystallization or melting temperature is reached. However, optimizing the reversible change of phase requires dealing with a multi-physics interplay between laser absorption, heat transfer and phase change dynamics.[27] The majority of studies on laser-induced phase transition in PCMs concentrate on image printing[15,28–30] as well as writing devices[31] such as gratings[32] or Fresnel zone-plates,[33,34] without in-depth description of all the underlying mechanisms involved in the reversible optical switch. Consequently, our work aims at gaining insights in the physical mechanisms at play when switching optically Sb_2S_3 by relating multi-physics (thermal, optical and phase change) simulations to experimental results.

Here, we focus on the reversible laser amorphization of Sb_2S_3 realized with a single-pulse laser, contrary to most reports where the phase transition is generally performed using several pulses.[28,35,36] Specifically, we determine the energy range for the reversible phase change of Sb_2S_3 both experimentally and via simulations. By comparing simulations to structural analysis carried out through TEM observation of the amorphized spots, we are able to gain understanding on the phenomena involved when optically switching Sb_2S_3. Furthermore, by investigating the laser recrystallization dynamics, we achieved the partial phase transition of Sb_2S_3. We also report the impact of Sb_2S_3 anisotropy on the laser-induced amorphization, and identify the limiting factors in optically programming thick Sb_2S_3 layers. Finally, we investigate the impact of the film thickness and, based on the simulations, we propose a strategy to switch thick films, which is often reported challenging.[27,37]

P. Thiesen, R. Bourrellier
Park Systems France
21 rue Jean Rostand, Orsay 91400, France

2. Laser Amorphization Principle and Theory

The phase transitions in PCM are temperature-time-dependent transformations. Typically, amorphization is the result of a melt-quench process demanding high temperature (above the melting point) to melt the PCM and short heating time so that the PCM quickly cools down without recrystallizing. Conversely, crystallization necessitates longer heating time at moderately high temperatures (below the melting point) to let the crystals form and grow. To induce these phase changes optically, the material is heated by laser irradiation: the light is substantially absorbed in the film depending on the PCM's optical properties, which translates into a localized temperature elevation. For a given laser wavelength, the type of phase transition (amorphization or crystallization) is determined by the laser power and exposure time as shown in **Figure 1a**.

Here, we focus on the reversible laser amorphization of Sb_2S_3 thin films exposed to a 532 nm laser at normal incidence, as illustrated in Figure 1b. This laser energy (2.33 eV) is over the bandgap of the crystalline Sb_2S_3 (1.75 eV) and it is absorbed by the amorphous Sb_2S_3. Examples of experimental demonstrations of the phase transition are provided in Figure 1c, representing an optical microscope top view of a 42 nm-thick Sb_2S_3 film in its two reference states (amorphous and crystallized) and after laser exposure (third image). The circular laser-amorphized region appears with the same purple color as the amorphous reference and is completely erased after laser recrystallization (fourth image). To better understand the physical mechanisms involved in the laser-induced amorphization of Sb_2S_3, we simulate the laser heating using an in-house multiphysics model combining optical and thermal simulations of the device.

2.1. Optical Simulation

The light absorbed within the stack containing the Sb_2S_3 thin film determines the amount of energy available for the phase transition and depends on the optical absorption of Sb_2S_3 as well as on the multiple reflections within the different layers. The optical behaviors of the stack (absorption, transmission, and reflection) under normal incidence are numerically calculated by employing the transfer matrix method.[38] The simulated stack consists in a silicon substrate, a 42 nm-thick Sb_2S_3 layer and a 30 nm-thick SiO_2 capping layer. The optical properties of the Sb_2S_3 and SiO_2 thin films (refractive index n and absorption coefficient k) used for the calculation are $n_{Sb_2S_3c} = 4.72 \pm 0.03$, $k_{Sb_2S_3c} = 0.74 \pm 0.04$, $n_{SiO_2} = 1.47$, and $k_{SiO_2} = 0$. These values were determined experimentally by ellipsometry measurements[19,20] and are displayed on Figure 1d for Sb_2S_3. The laser wavelength is fixed at the experimental value of 532 nm. Since the simulated profile is obtained by performing 1D simulations, the spot size is not directly included in the calculation. Instead, the laser pulse

© 2024 The Author(s). Advanced Optical Materials published by Wiley-VCH GmbH

21951071, 2024, 28, Downloaded from https://advanced.onlinelibrary.wiley.com/doi/10.1002/adom.202401214 by Universidad De Cantabria, Wiley Online Library on [18/02/2025]. See the Terms and Conditions (https://onlinelibrary.wiley.com/terms-and-conditions) on Wiley Online Library for rules of use; OA articles are governed by the applicable Creative Commons License

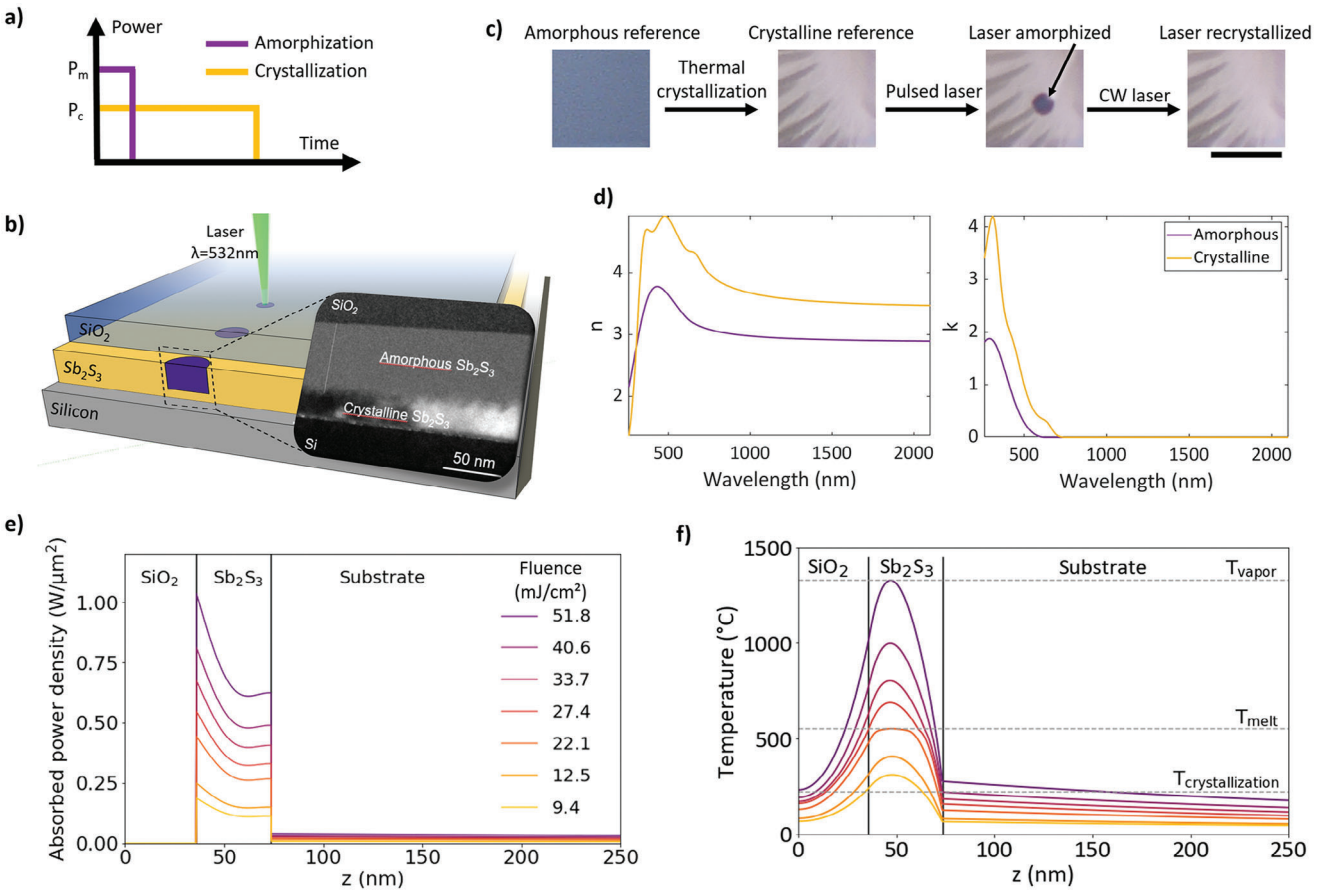

Figure 1. Optical switch principle a) laser pulse profile for each phase transition, b) schematic of Sb_2S_3 optical switch principle, with a close-up view of a TEM observation of a partially amorphized Sb_2S_3 layer, c) optical microscope image of the 42 nm-thick Sb_2S_3 sample in its different states (scale bar: 20 μm), d) Sb_2S_3 optical index in the crystalline and amorphous phase (measured for a 42 nm thick Sb_2S_3 layer, e,f) simulated optical absorption and corresponding temperature profile at the end of the 500 ps pulse along the stack, for a 42 nm-thick Sb_2S_3 layer, plotted for several values of laser pulse fluence.

fluence is used to calculate the expected absorbed power density in the stack from the integration of the Poynting vector. The resulting absorbed power density profile, shown in Figure 1e, does not vary uniformly across the Sb_2S_3 layer: it decreases sharply in the first 25 nm of the PCM before holding steady and slightly increasing in the last nanometers. This is an expected result from the stack geometry, which produces standing waves in the PCM layer. Naturally, increasing the laser fluence also leads to higher absorbed power density. The resulting absorption profile is then used for solving the heat equation and obtaining the corresponding temperature throughout the film, as explained in detail in the following.

2.2. Thermal Simulation

The temperature profile in the stack, illustrated in Figure 1f, is obtained by solving the 1D heat equation in the structure:

$$\rho C_p \frac{\partial T}{\partial t} = \frac{\partial}{\partial z}\left(\kappa \frac{\partial T}{\partial z}\right) + Q \tag{1}$$

where ρ is the density, C_p is the specific heat capacity at constant pressure, T is the temperature, t is the time, z is the distance to the surface of the sample, κ is the thermal conductivity and Q is the absorbed power density calculated in the optical simulation as explained above. For the calculation, the bottom temperature of the substrate is fixed at room temperature and the top surface is considered as thermally isolated ($\frac{\partial T}{\partial x} = 0$). The lateral heat transfer is not taken into account in the 1D simulations, and the thermal boundary resistances from layer to layer are also ignored due to the lack of experimental data.

As the thermal simulation progresses, the PCM temperature is monitored (see **Figure 2**), so as to interrupt the simulation as soon as the melting temperature is attained in any location within the PCM layer. When it does occur, the layer structure is updated to account for the newly melted region, for which amorphous material properties are assumed, and a new optical simulation is run. This sequential multi-physics simulation continues along the duration of the single pulse. In order to account for the latent heat of fusion, the specific heat of crystalline Sb_2S_3 is adjusted right below the melting point. This predictably leads to a plateauing effect near T_{melt}, as can be observed in Figure 2 illustrating

© 2024 The Author(s). Advanced Optical Materials published by Wiley-VCH GmbH

21951071, 2024, 28, Downloaded from https://advanced.onlinelibrary.wiley.com/doi/10.1002/adom.202401214 by Universidad De Cantabria, Wiley Online Library on [18/02/2025]. See the Terms and Conditions (https://onlinelibrary.wiley.com/terms-and-conditions) on Wiley Online Library for rules of use; OA articles are governed by the applicable Creative Commons License

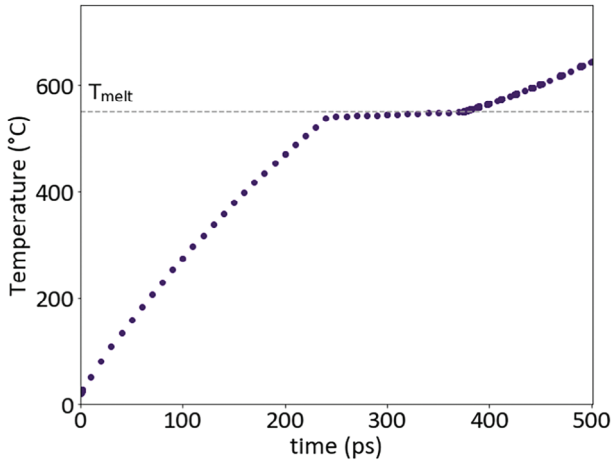

Figure 2. Maximum simulated temperature in the PCM film taken every 10 ps during the entire duration of the pulse, for a 27.4 mJ cm^{-2} pulse fluence.

the temperature rise in the PCM film throughout the duration of the pulse.

Figure 1f shows examples of temperature profiles calculated across the depth of the 42 nm-thick Sb_2S_3 sample against laser fluence, for a fixed pulse duration of 500 ps (chosen to match our experimental conditions). The calculated temperature profile within the stack takes on a bell shape that is markedly different from the optical absorbed power density profile (see Figure 1e,f), showing the non-negligible impact of heat transfer. Note that the peak temperature is located closer to the capping than the substrate. This is because most of the heat is evacuated through the highly thermally-conductive Si layer, whereas the thin SiO_2 capping layer acts as a temporary heat store since it is thermally insulated. Consequently, Sb_2S_3 starts amorphizing at the location of the peak temperature and the amorphized region subsequently spreads across the PCM layer. The melting temperature is first reached 10 nm below the capping/Sb_2S_3 interface, for a laser fluence of at least 22 mJ cm^{-2}. The top surface of the PCM then starts to melt for a laser fluence of 27.4 mJ cm^{-2}. By further increasing the laser power, a larger fraction of the material can be amorphized, but, for a laser fluence above 51.8 mJ cm^{-2}, the peak temperature reaches the evaporation point of Sb_2S_3. We consider this fluence (51.8 mJ cm^{-2}) as a threshold limit before damaging the PCM layer. The fluence window for amorphizing Sb_2S_3 thus spans from 22 to 51.8 mJ cm^{-2}. For a lower pulse fluence (between 22 and 27.4 mJ cm^{-2}) the PCM layer has a crystalline-amorphous-crystalline structure, while a higher fluence (between 27.4 and 51.8 mJ cm^{-2}) results in an amorphous-crystalline structure. For the specific case presented here, the film is never fully amorphized: at most, the amorphized depth is 34 nm when the maximum temperature reaches the evaporation point. Not fully amorphizing the film could limit the applications of Sb_2S_3, hence the need for thorough experimental verification of these results.

3. Experimental Results

We describe in the following the experimental demonstrations of reversible laser amorphization of a 42 nm-thick Sb_2S_3 film. The PCM is deposited amorphous on a silicon substrate by electron beam evaporation and capped with a SiO_2 layer (30 nm-thick) to prevent oxidation.[39] The amorphous as-deposited Sb_2S_3 layer is then thermally crystallized under ambient conditions at 280 °C for two hours (cf. ellipsometry curves Figure 1d; XRD and Raman spectra in Figures S1 and S4, Supporting Information), before being laser amorphized. The reversibility of the laser amorphization is verified by recrystallizing the PCM as mentioned previously (see Figure 1c).

3.1. Laser Switching Optical Setup

The optical setup used for the laser-induced phase transition is illustrated in **Figure 3**. Amorphization is realized using a laser with a fixed pulse duration of 500 ps, while recrystallization of the amorphized spots is performed with a continuous wave (CW) laser. The two lasers have the same wavelength: 532 nm, and are focused over a spot having a 5 µm waist on the top surface of the sample. An acousto-optic modulator (AOM) controlled by a function generator and a LabView program enables: 1) selecting a single laser pulse for amorphization, 2) defining the exposure time of the continuous laser for recrystallization, and 3) tuning both laser powers.

3.2. Laser Amorphization

To experimentally determine the minimum laser fluence for amorphizing the Sb_2S_3 sample, we sweep the laser power and first rely on colorimetric observations for identifying amorphized regions. Given the different optical properties of the two phases, amorphized spots should appear in different colors than their surroundings when observed under an optical microscope. The results are provided in **Figure 4a**, where the optical microscope images of the sample's top surface are displayed as a function of the pulse energy. For energy between 10 and 26 nJ, the purple color of the amorphized Sb_2S_3 is clearly distinguishable and the refractive index of these purple spots were found to be very close to that of the as-deposited amorphous reference (see ellipsometry data in Section S3, Sup porting Information). Below 10 nJ, no change on the film surface compared to the crystalline reference is noticeable. Above 26 nJ, the center of the spot exhibits a dark color that cannot be recrystallized. We concluded that the surface of the sample starts to be damaged and is eventually ablated when the laser energy is further increased. This damage corresponds to a swelling of the film (see AFM characterization in Section S2, Supporting Information), and is likely due to the thermal expansion of the PCM under excessive heating. As the capping layer can no longer accommodate for the PCM's volume change it is irremediably pushed away, resulting in the film's ablation. For amorphizing Sb_2S_3, the laser energy thus should be kept between 10 and 26 nJ.

We also notice subtle changes within this amorphizaton window: the amorphized region expands and the spot color becomes more saturated as we increase the laser pulse energy. We tentatively ascribe this tendency to a partial amorphization for low-energy spots, as predicted by the simulations. The spot size dependency to the pulse energy is attributed to the Gaussian profile

© 2024 The Author(s). Advanced Optical Materials published by Wiley-VCH GmbH

21951071, 2024, 28, Downloaded from https://advanced.onlinelibrary.wiley.com/doi/10.1002/adom.202401214 by Universidad De Cantabria, Wiley Online Library on [18/02/2025]. See the Terms and Conditions (https://onlinelibrary.wiley.com/terms-and-conditions) on Wiley Online Library for rules of use; OA articles are governed by the applicable Creative Commons License

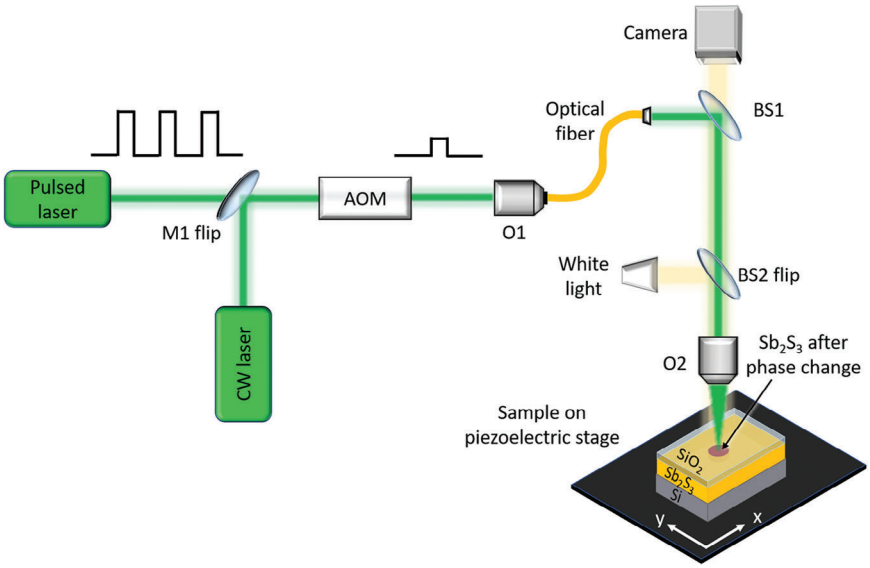

Figure 3. Optical set-up used for the reversible phase transition of the PCMs.

of the beam: since the laser intensity is the highest in the center of the spot, this area would reach the melting point before the edges of the spot do. As a consequence, for the spots obtained with a low pulse energy, only the center of the beam is powerful enough to melt Sb_2S_3, while for high energies nearly all the surface of the beam provides enough power for amorphization, as illustrated in Figure 4b. We can extract the experimental amorphization fluence threshold by measuring the spots diameters as a function of the laser energy and calculating the corresponding intensity at the edge of the spot using the Gaussian beam formula:

$$F(r) = \frac{2E}{\pi w_0^2} exp(\frac{-2r^2}{w_0^2}) \quad (2)$$

where F is the laser fluence, E is the measured pulse energy arriving on the sample, w_0 is the beam waist (here 5 µm) and r is the distance to the center of the beam spot. These results are given in Figure 4c for six different pulse energies. Using this method, the experimental amorphization threshold was found to be between 21 and 29 mJ cm^{-2}, which is in good agreement with the simulations. The variability of the values can be attributed to the measurement errors on the laser energy (1 nJ) and spot diameter (0.5 µm), as well as to the material's anisotropy as will be discussed further. The damage threshold is harder to estimate as the shape of the damaged area is more unpredictable. It should however lie between 67 (maximum of the Gaussian for 26 nJ laser energy) and 79 mJ cm^{-2} (maximum of the Gaussian for the 32 nJ spot). In this case, the damage threshold was under-estimated by the simulations.

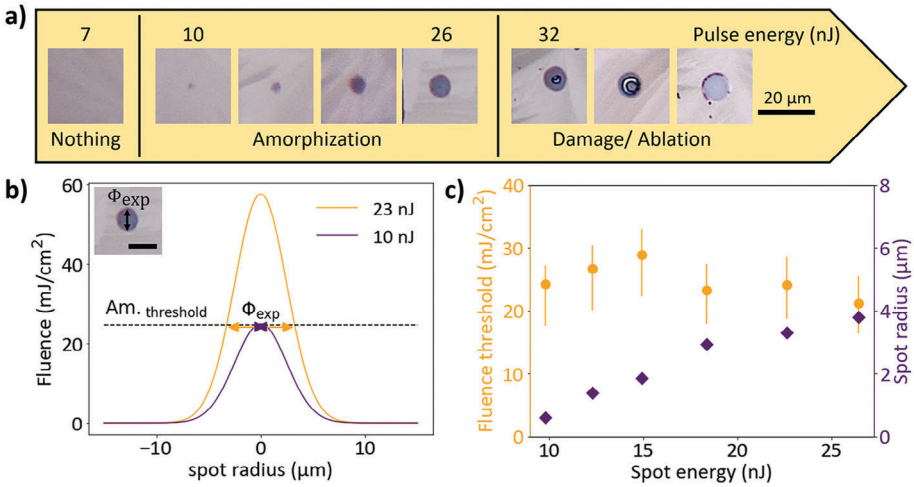

Figure 4. Determination of the minimum fluence threshold for amorphization with a) optical microscope images of the spot as a function of the pulse energy, b) example of the calculated Gaussian profile of the spot for two different pulse energies, and c) spot radius and fluence threshold as a function of the pulse energy. The error bars on the amorphization threshold are calculated with the combined uncertainty on the spot diameters and pulse energy measurements.

 © 2024 The Author(s). Advanced Optical Materials published by Wiley-VCH GmbH

21951071, 2024, 28, Downloaded from https://advanced.onlinelibrary.wiley.com/doi/10.1002/adom.202401214 by Universidad De Cantabria, Wiley Online Library on [18/02/2025]. See the Terms and Conditions (https://onlinelibrary.wiley.com/terms-and-conditions) on Wiley Online Library for rules of use; OA articles are governed by the applicable Creative Commons License

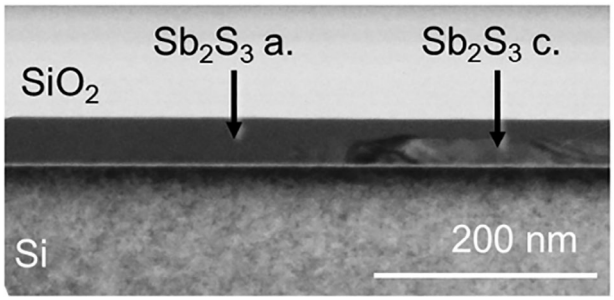

Figure 5. TEM cross-section of an amorphized spot observed in bright field mode on the 42-nm-thick Sb_2S_3 layer.

We now want to investigate the depth of the amorphization spots. As mentioned before, the low power spots appear in lighter color compared to the amorphous reference, which suggests partial amorphization. Additionally, from the simulation, the maximum depth that could be amorphized is 34 nm. Consequently, although a simple color comparison allows to know if the phase transition occurred, the thickness of the change of phase remains imprecise. To gain insights on the amorphization depth, a TEM cross-section of the spot was performed and the edge of the amorphized region is shown in **Figure 5**. The observed spot was obtained with the highest possible laser power below the damage threshold to maximize the chance of amorphizing the sample down to the substrate. As displayed in Figure 5, the TEM observation confirms that the Sb_2S_3 layer was completely amorphized in the center of the spot, contrary to the simulations prediction, with the amorphous region appearing homogeneous as a result of no diffraction contrast. The Gaussian shape of the beam is also visible at the edge of the spot and, as predicted by the simulations, the amorphization starts close to the surface and extends in the PCM's depth. This observation thus confirms the analysis presented above as well as the possibility to fully amorphize 42 nm of Sb_2S_3. It is also a clear demonstration that our simulations provide a good description of the physical mechanisms involved in laser-induced amorphization. The slight differences with the experiments are attributed to experimental uncertainties and simulation hypothesis. Indeed, only 1D simulations were performed and thus neither the Gaussian profile of the beam nor the heat dissipation on the sides (in x and y directions) were taken into account. These approximations probably induce discrepancies in the results.

3.3. Laser Recrystallization

As the amorphization window has been found, the same study can be conducted for the laser-induced recrystallization of Sb_2S_3 in order to find the optimum parameters for the reversible phase transition. The material was first amorphized with the highest possible energy below the damage threshold to guarantee a complete phase transition on the widest possible area (see inset 3, **Figure 6a**). It was assumed that all amorphized regions made with the same pulse energy are comparable. The amorphized spots are then exposed to the CW laser, with varying exposure time and power. The objective is to find the minimum time/energy set to completely recrystallize the spot. To do so, for a given laser power, the spots were exposed to the CW laser for various exposure times (with a time-step difference of 2 ms) and the surface of the sample was observed under the optical microscope to verify the recrystallization of the spots. A spot is recrystallized when the purple amorphized region is no longer visible as seen on inset 1, Figure 6a (cf. Raman measurement in Section S4, Supporting Information). The exposure time was thus increased until the amorphized spots completely disappear and the surface of the sample appears fully crystalline under the optical microscope. This process was conducted for several laser powers.

Figure 6a displays the minimum exposure time needed to achieve the full laser recrystallization of amorphized spots (inset 1) as a function of the laser power. The results are unambiguous: the higher the power, the faster the recrystallization time. Indeed, the time needed to fully recrystallize the amorphous spot for a 1 mW laser power is 600 ms, while it becomes 7 ms for a 30 mW laser pulse. The most straightforward explanation for this would be energy conservation: considering there is a minimum activation energy to recrystallize the laser-amorphized region, the same total energy can be obtained by compensating a decreased laser

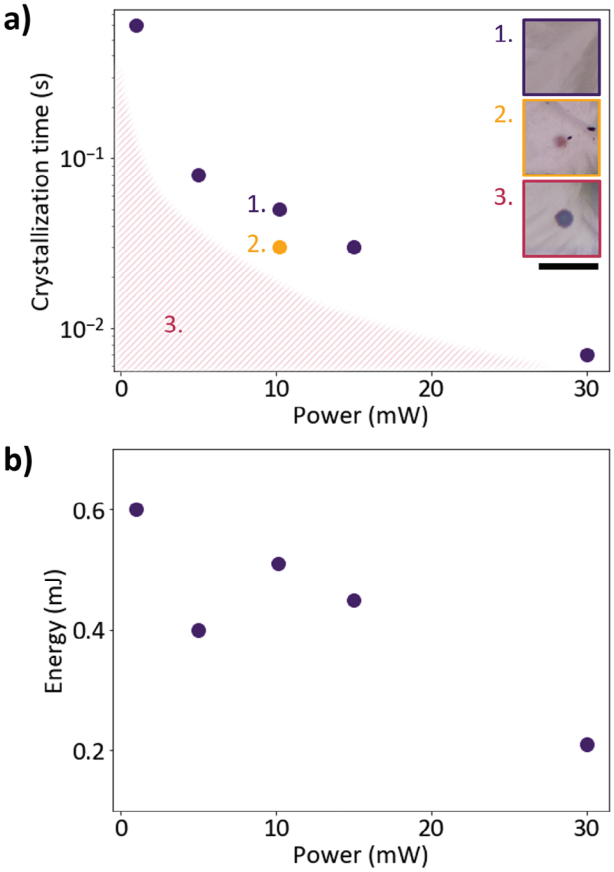

Figure 6. Minimum recrystallization time a) and energy b) as a function of the laser power (in dark purple). The yellow dot in a) is an example of power and time combination to achieve partial recrystallization and the inset represents the microscope views of the sample's surface with a fully-recrystallized (1), a partially recrystallized (2) and an initial amorphized (3) spots for the corresponding data points on the graph (scale bar: 20 µm) - Note that the dots represent the actual experimental values, while the colored dashed part is an estimation of the limits for recrystallization.

© 2024 The Author(s). Advanced Optical Materials published by Wiley-VCH GmbH

21951071, 2024, 28, Downloaded from https://advanced.onlinelibrary.wiley.com/doi/10.1002/adom.202401214 by Universidad De Cantabria, Wiley Online Library on [18/02/2025]. See the Terms and Conditions (https://onlinelibrary.wiley.com/terms-and-conditions) on Wiley Online Library for rules of use; OA articles are governed by the applicable Creative Commons License

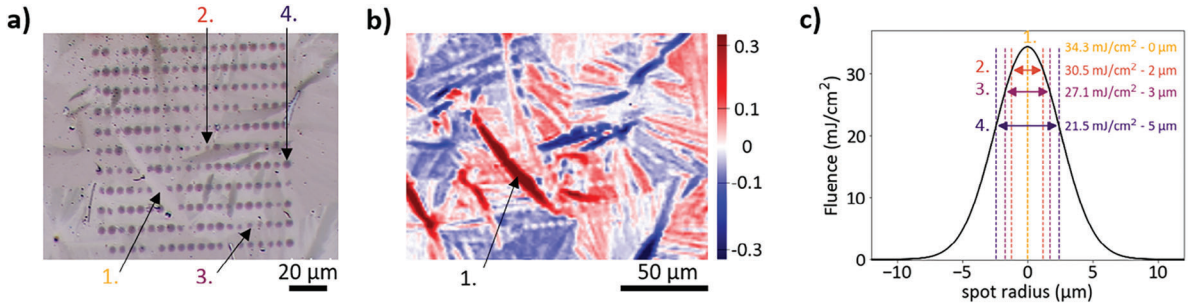

Figure 7. Impact of the anisotropy on amorphization reproducibility shown with a) the optical microscope images and b) the Mueller matrix element M13 of a grid of amorphized spot made with a 13.5 nJ laser pulse on 42 nm-thick Sb_2S_3 layer. c) Measured diameters of a few spots and corresponding fluence threshold displayed on the calculated Gaussian beam profile for the 13.5 nJ laser pulse.

power with an increased exposure time. Yet, the experimental values of power and recrystallization time do not yield a constant energy (see Figure 6b), suggesting the existence of an additional factor explaining the observed trend. As we explain in the following, this may be due to the crystallization kinetics of Sb_2S_3. We showed in a previous work[20] that the crystallization dynamics of Sb_2S_3 follows the Avrami's law, which states that the crystallization is faster as the temperature increases. This theory takes into account the two steps of crystallization: nucleation and subsequent growth of the grains.[40] Here, the amorphized spots are surrounded by a crystalline matrix, therefore recrystallization just consists in grain growth. From the crystallization theory,[41] the grain growth rate of the crystal $u(T)$ as a function of the temperature T is expressed as follows:

$$u(T) = f.D(1 - e^{\frac{-\Delta G}{R.T}}) \tag{3}$$

where f accounts for the surface roughness, D is the diffusivity accounting for atomic mobility, G is the thermodynamic driving force and R is the gas constant. From this equation, we see that when the temperature increases, the grain growth is faster. Considering that the temperature inside the Sb_2S_3 thin film directly increases with higher laser power, the trend in Figure 6 can be explained by PCM crystallization kinetics.

Using these results and the crystallization theory, it is then possible to achieve partial phase transitions of the material by stopping the recrystallization before it is complete, as shown in inset 2, Figure 6a. This partially recrystallized spot was obtained by reducing the exposure time from 50 ms (full recrystallization) to 30 ms for a 10 mW laser pulse (yellow dot in Figure 6a). It is thus possible to program several partially recrystallized states in the depth of the PCM, which is promising for multi-level applications such as grayscale lithography and neuromorphic computing. Additionally, contrary to the laser amorphization, the shape of partially recrystallized spots should not be impacted by the beam profile, as the phase transition is primarily governed by the crystallization dynamics of Sb_2S_3. Thus this method seems more promising for controlling the partial phase transition than the usual partial amorphization obtained via increasing the number of pulses. All these results show that the laser amorphization of Sb_2S_3 is reversible, and, although we did not carry out a full endurance test, the reversible switching could actually be performed over ten cycles.

4. Discussion

4.1. Reproducibility and Impact of the Material's Polycrystallinity

Exploring the reproducibility of the laser-induced phase transition of Sb_2S_3 is of major importance for the future integration and scalability of this PCM on devices. To check the reproducibility of our switching method, arrays of 20×11 amorphization spots were made on the 42 nm-thick Sb_2S_3 for several laser powers. An example of such a grid of spots is given in **Figure 7** for a 13.5 nJ laser pulse. It is clear from the optical microscope view of the sample's surface that the spot sizes are position-dependent (cf. Figure 7a). Here, it is important to remember that the thermal crystallization of Sb_2S_3 results in a randomly oriented polycrystalline layer. As Sb_2S_3 crystallizes in an orthorhombic structure, it is anisotropic and its optical properties are therefore orientation-dependent.[42] Then, due to the polycrystallinity and occurrence of several orientations in the Sb_2S_3, the layer is also anisotropic with position-dependent properties. This appears clearly on the different microscope images of the sample displayed previously, with large grains of different contrasts, similar to previous reports.[28,43,44] In Figure 7a, we notice a correlation between the size of amorphous spots and crystal grain orientations. This observation indicates that the amorphization threshold is impacted by the crystal grain's orientation on which it is performed. Specifically, amorphization did not occur on the grain located at the lower left part of the spot grid (identified as 1) in Figure 7a.

The Mueller matrix element m13 of the same region in Figure 7b clearly highlights the anisotropy of Sb_2S_3, which is characterized by non-zero values (colored region—see the Experimental Section and Section S5, Supporting Information, for more information). The grain on which amorphization did not occur appears in dark red, thus showing high anisotropy (see arrow 1 in Figure 7b, while the amorphized spots appear as white and are therefore isotropic. Given the temperature within the Sb_2S_3 layer is determined by both the thermal properties of the material and its optical absorption profile, the anisotropy of Sb_2S_3 consequently affects the amorphization threshold through a modification of the optical absorption. So far, the importance of this property of the PCM comparatively to other impacting parameters on the amorphization has not been precisely quantified. By measuring several spot diameters and calculating the corresponding fluence threshold, it appears that the latter

© 2024 The Author(s). Advanced Optical Materials published by Wiley-VCH GmbH

21951071, 2024, 28, Downloaded from https://advanced.onlinelibrary.wiley.com/doi/10.1002/adom.202401214 by Universidad De Cantabria, Wiley Online Library on [18/02/2025]. See the Terms and Conditions (https://onlinelibrary.wiley.com/terms-and-conditions) on Wiley Online Library for rules of use; OA articles are governed by the applicable Creative Commons License

Table 1. Amorphization and damage fluence threshold in mJ cm^{-2} extracted from the thermo-optical simulations (sim.) and from the experimental Gaussian beam profile (exp.).

	Sim. fluence [mJ cm^{-2}]		Exp. fluence [mJ cm^{-2}]	
	Amorphization $T_{max} = T_{melt}$	Damage $T_{max} = T_{evap}$	Amorphization	Damage
31 nm	26	71	21 - 32	>95 - <106
42 nm	22	52	21 - 29	>67 - <79
93 nm	19	39	18 - 21	>51 - <68
175 nm	18	40	20 - 22	>65 - <74

fluctuates between 22 and at least 34 mJ cm^{-2} (see Figure 7c, the considered spots are marked on Figure 7a). The fluence window for amorphization is therefore strongly affected by the anisotropy and polycrystallinity of Sb_2S_3, as it can induce a variation of amorphization threshold up to 36% of the overall amorphization window. This parameter thus seems to be the most impacting one when performing the optical switch of Sb_2S_3 and makes it hard to conclude on the impact of other parameters whose variability is typically lower. Although it was not precisely quantified, the polycrystallinity of the film should also have a similar impact on the laser-induced recrystallization. Consequently, the optimal laser power for the reversible amorphization should be calibrated for each grain with a local optical dispersion measurement.

4.2. Impact of the Film Thickness

So far we have only discussed the reversible laser amorphization of a 42 nm-thick film of Sb_2S_3. However, for free space nanophotonic applications such as metasufaces, thicker films, typically of several hundred nanometers, are often needed to achieve the desired functionality. Yet, the optical switching of thick PCM films is often reported as a challenging task,[27,37] thus underlining the necessity to study the impact of the Sb_2S_3 thickness on the laser amorphization.

We investigate the laser amorphization of Sb_2S_3 films with thicknesses ranging from 31 to 175 nm. The thicknesses of PCM layers were chosen to lie within the standard values used for applications in integrated nanophotonics, i.e., in the range 20–200 nm. All samples have been fabricated and amorphized using the method presented in the previous sections. **Figure 8a** presents the optical microscope images of spots realized on four Sb_2S_3 thin films using the maximum laser power before damage. As evidenced by the color change, all samples could be amorphized, regardless of their thickness. The window ranges necessary for amorphization have been determined from the simulations as well as experimentally, as explained in Section 3.2, and are given in **Table 1**. From the simulations, both the amorphization and damage thresholds slightly decrease when increasing the film thickness. This can be attributed to the lower thermal conductivity of Sb_2S_3 compared to the silicon substrate: the Sb_2S_3 layer acts as a resistance to heat dissipation toward the substrate. When increasing Sb_2S_3 thickness, the heat leakage in the substrate is thus mitigated, hence reducing the energy needed to reach a given temperature. This effect was also reported for Sb_2Se_3 by Lawson et al.[27] Experimentally, this trend does not appear as clearly, except for the damage threshold of the thinner film. The fact that all films seem to have more or less the same amorphization and damage thresholds, is attributed to the large uncertainty on the determination of the thresholds. This could be a consequence of the film's anisotropy: it was shown previously that the amorphization threshold could vary by nearly 13 mJ cm^{-2} depending on the position on the Sb_2S_3 grain.

Nevertheless, increasing the film thickness still induces a difference in the results: the thick films could not be completely amorphized. Indeed, the spots on the Sb_2S_3 films thicker than 42 nm present different colors than the as-deposited amorphous reference, as shown in Figure 8a. Additionally, the crystal grains are visible below the spots for these layer thicknesses, suggesting that the films are just partially amorphized. It is possible to estimate the amorphized thickness by colorimetry analysis: we compare the spot color to the simulated reflected color of the stack, as calculated by coupling the reflectivity from the transfer matrix with color matching functions (more details in ref. [45]). An example of such analysis is displayed in Figure 8b for the 93 nm sample. The simulated reflected colors for the stack Si (substrate)/Sb_2S_3 c/Sb_2S_3 a/SiO_2(30 nm), are presented in Figure 8b as a function of the amorphous Sb_2S_3 thickness (the overall Sb_2S_3 thickness being 93 nm). From the color of the experimentally measured spot, we estimate an amorphized thickness that lies between 45 and 55 nm for this sample. This hypothesis is verified by TEM observations. Indeed, to verify precisely the amorphized thickness, we have conducted a TEM analysis of the spot made on the 93 nm-thick film. Figure 8c displays the center of the spot cross-section TEM dark-field image, where the crystallinity is illustrated by a strong diffraction contrast and the maximum amorphized thickness is 66 nm in the center of the spot. The amorphous to the crystalline interface being rough, the amorphized thickness can only be estimated within ≈10 nm precision. The underestimation of the amorphized thickness from the color simulation could be due to this roughness as well as to a potential volume change upon phase transition. These results indicate the existence of a maximum Sb_2S_3 thickness that can possibly be amorphized in this particular configuration of laser and sample. This phenomenon has also been observed by other groups[27,34] and is commonly referred to as the thickness limit.[37] It is essential to overcome this thickness limit in order to optimize the potential of Sb_2S_3 for various nanophotonic applications.

4.3. Insights on Overcoming the Thickness Limit

Successful laser amorphization is the result of a competition between several physical phenomena: the recrystallization kinetics,

© 2024 The Author(s). Advanced Optical Materials published by Wiley-VCH GmbH

21951071, 2024, 28, Downloaded from https://advanced.onlinelibrary.wiley.com/doi/10.1002/adom.202401214 by Universidad De Cantabria, Wiley Online Library on [18/02/2025]. See the Terms and Conditions (https://onlinelibrary.wiley.com/terms-and-conditions) on Wiley Online Library for rules of use; OA articles are governed by the applicable Creative Commons License

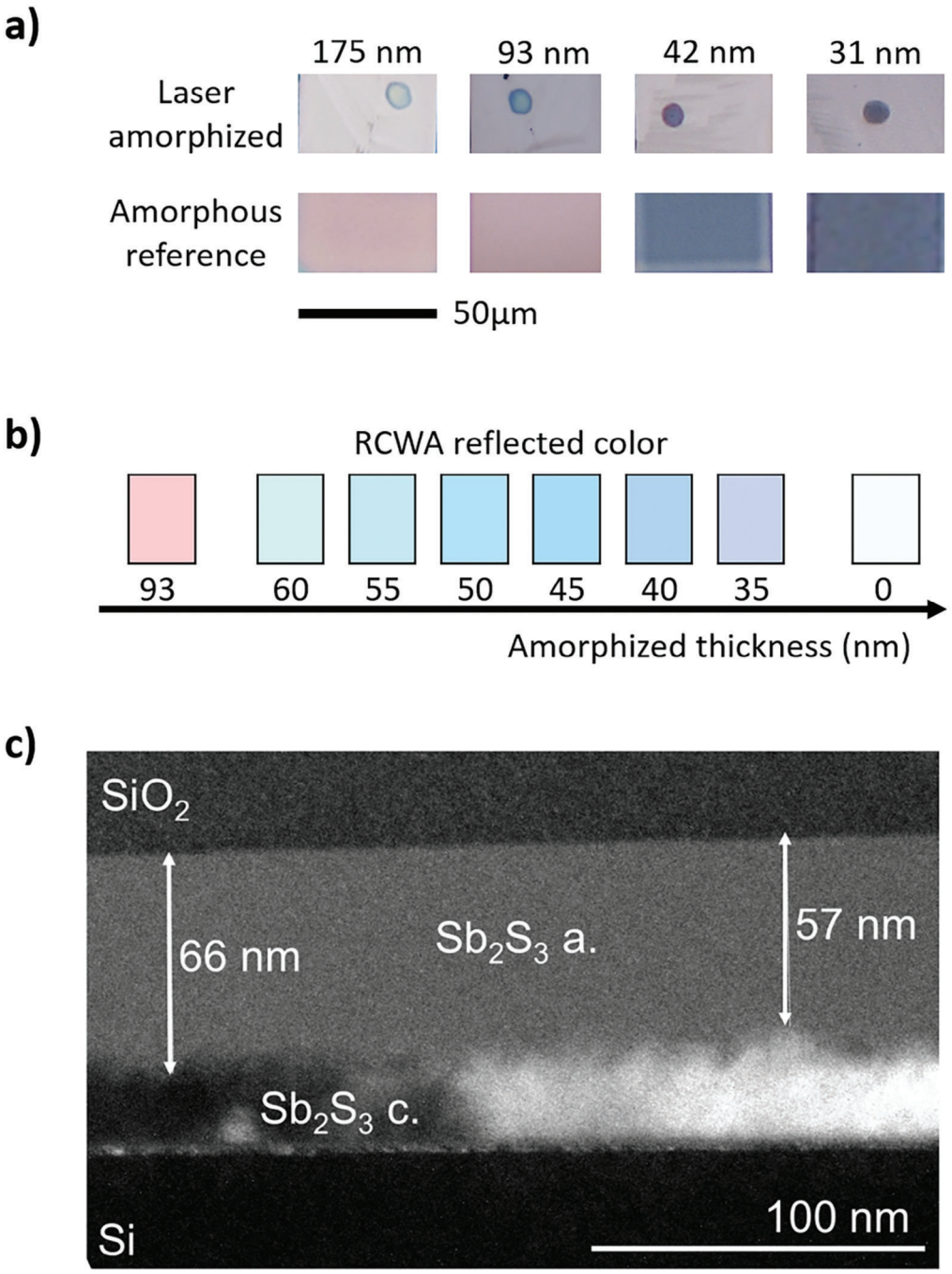

Figure 8. Amorphization of thick films: a) optical microscope image of laser amorphized and as-deposited amorphous sample of different thickness of Sb_2S_3 b) simulated colors of the stack Si substrate/Sb_2S_3 c/ Sb_2S_3 a/ SiO_2 (30 nm) for varying amorphized thicknesses on the 93 nm Sb_2S_3 sample c) TEM cross-section of the laser amorphized spot on the 93 nm-thick Sb_2S_3 sample observed in the dark field mode.

the thermal properties of the stack and the optical absorption. A commonly given explanation for the thickness limit is the interplay between the thermal conductivity and the critical cooling rate of the PCM.[37] However, we show in this section that the optical absorption is the limiting aspect when amorphizing our thick Sb_2S_3 films and the maximum amorphized thickness can be increased by optimizing the absorption profile.

For amorphization to occur, the material must be melt-quenched fast enough to suppress crystallization. The critical cooling rate Θ_{crit} is defined as the minimum quenching rate preventing crystallization: $\Theta_{crit} = \frac{\Delta T}{\tau_{min}}$ where τ_{min} is the minimum crystallization time, and ΔT is the temperature difference between the melting point T_{melt} and the temperature at which crystallization is the fastest T_{nose}.[41,46] It has been reported that for

© 2024 The Author(s). Advanced Optical Materials published by Wiley-VCH GmbH

21951071, 2024, 28, Downloaded from https://advanced.onlinelibrary.wiley.com/doi/10.1002/adom.202401214 by Universidad De Cantabria, Wiley Online Library on [18/02/2025]. See the Terms and Conditions (https://onlinelibrary.wiley.com/terms-and-conditions) on Wiley Online Library for rules of use; OA articles are governed by the applicable Creative Commons License

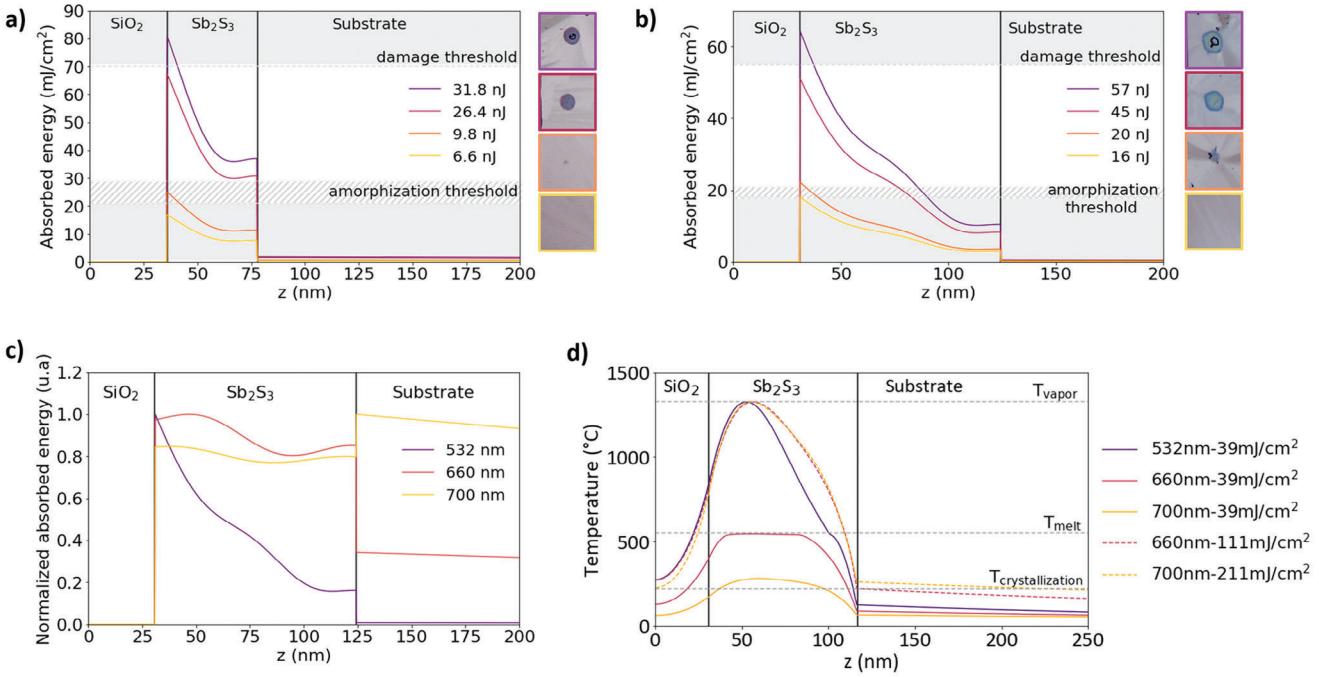

Figure 9. Simulated optical absorption at 532 nm in the center of the spot for different laser energy for the thin film of a) 42 nm and b) 93 nm of Sb_2S_3 and corresponding top view of the spots. Impact of laser wavelength on c) the normalized optical absorption profile and d) the temperature profile throughout the sample.

thick films, the PCM thermal conductivity is the limitation to this critical cooling rate as it can hinder the heat evacuation out of the PCM. Considering only the PCM thermal conductivity, the thickness limit t_{max} can be expressed as a function of the critical cooling rate as follows:[27]

$$t_{max} \approx \sqrt{\frac{\alpha.\Delta T}{\Theta_{crit}}} = \sqrt{\alpha.\tau_{min}} \quad (4)$$

where α, the thermal diffusivity ($\alpha=\kappa/(C_p.\rho)$) is assumed constant within the PCM. For Sb_2S_3, taking $\tau_{min} = 7$ ms, our minimum experimental crystallization time, the calculated thickness limit is 70 µm, which is much larger than the thickness of the films considered in the present work. One could argue that the minimum crystallization can be smaller when using high-energy amorphization pulses. Yet, the smallest crystallization time reported is a few µs, which would give a thickness limit around 800 nm. These results could vary a bit with different values of thermal diffusivity but would not change the conclusions presented here. Additionally, our laser pulse duration (500 ps) being much smaller than this minimum crystallization time and the use of Si substrate helping heat evacuation make it very unlikely for Sb_2S_3 crystallization kinetics to be the reason for thick film partial amorphization.

On the other hand, we explain in the following that the main obstacle for amorphizing thick layers is the strong optical absorption of Sb_2S_3. Indeed, as explained before, in optically induced phase transitions, the optical absorption directly determines the amount of energy available for the transition to occur. **Figure 9**a,b displays the profile of absorbed energy respectively in the 42 and 93 nm-thick Sb_2S_3, calculated for several laser powers. When comparing the results to the experimental amorphization window (limits in grey on the graphs) for the two samples, it appears that, at laser energies close to the damage threshold, the absorbed laser power remains above the amorphization threshold throughout the film for the 42 nm-thick film while it goes below the amorphization threshold in the last 37 nm for the 92 nm-thick film. For this latter film, we conclude that it is not possible to fully amorphize it in these conditions, as the absorbed energy decreases too sharply within the film. Thus, the absorbed energy density in the last 37 nm ends up below the amorphization threshold when the center of the spot starts to be damaged. One way to overcome this optical thickness limit would be to flatten the absorption profile. This could be realized by shifting to laser wavelengths that are less absorbed by Sb_2S_3. Figure 9c shows that by increasing the laser wavelength up to 660 nm, the absorbed energy profile is smoothed out. The thermo-optical simulations in Figure 9d demonstrate that the resulting temperature profile also flattens when increasing the laser wavelength. It results in an amorphized thickness increasing from 69 (wavelength of 532 nm) to 79 nm (wavelengths of 660 and 700 nm), by scaling up the laser energy to have the same maximal temperature for all laser wavelengths. Recently, Gao et al. demonstrated experimentally that 70 nm-thick Sb_2S_3 on glass could not be amorphized completely with a 480 nm laser, while amorphization was reported to be total when using a 550 nm laser,[34] which corroborates our theory. The downside of this method is that more energy is absorbed in the substrate due to the lower imaginary part of the Sb_2S_3 refractive index at these wavelengths as evidenced in Figure 9c. This consideration explains the drastic increase of laser fluence necessary to reach a given temperature. Indeed, from the thermo-optical simulation the laser energy density had to be

© 2024 The Author(s). Advanced Optical Materials published by Wiley-VCH GmbH

21951071, 2024, 28, Downloaded from https://advanced.onlinelibrary.wiley.com/doi/10.1002/adom.202401214 by Universidad De Cantabria, Wiley Online Library on [18/02/2025]. See the Terms and Conditions (https://onlinelibrary.wiley.com/terms-and-conditions) on Wiley Online Library for rules of use; OA articles are governed by the applicable Creative Commons License

increased from 39 to 111 mJ cm^{-2} and 211 mJ cm^{-2}, respectively at 660 and 700 nm, for the maximum temperature in the PCM to be the same as with the 532 nm pulse.

This analysis revealing that the bottleneck for the thickness limit of amorphization is not due to intrinsic thermal properties of Sb_2S_3 is actually encouraging. Indeed, increasing the thickness limit of amorphization is therefore a matter of engineering the optical and thermal environment of Sb_2S_3 so as to optimize the absorption and heat distribution within the PCM layer.

5. Conclusion

The reversible laser amorphization of Sb_2S_3 layers of various thicknesses was successfully demonstrated. The experimental results were related to multi-physics simulations for a better understanding of the underlying phenomena involved in the optically induced phase transition of Sb_2S_3. The experimental amorphization fluence threshold was found to be between 18 and 29 mJ cm^{-2}, while the films started to be irreversibly damaged for laser energy density above 51 mJ cm^{-2}. Overall, the thermo-optical simulations were in good agreement with these results, validating the proposed theoretical model. There was no significant impact of the thin film thickness on the amorphization energy window. However, films thicker than 42 nm could not be completely amorphized contrarily to the thinner films. This limitation was attributed to the sharpness of the optical absorption profile in the depth of the PCM and could be overcome by increasing the laser wavelength up to 660 nm. Additionally, we report the strong impact of the polycrystallinity and anisotropy of Sb_2S_3 on the amorphization results. This polycrystallinity induced a 36% variation in the value of the amorphization threshold, which is higher than the variability induced by the film thickness. Controlling the local optical absorption is thus of major importance for optimizing Sb_2S_3 laser amorphization since it was found to be the most impactful parameter. Regarding the recrystallization of the spots, full recrystallization was performed with a minimum time of 7 ms for a 30 mW laser power. The recrystallization time decreased exponentially when increasing the laser power, suggesting that the minimum recrystallization time could be further lowered by using a laser with a higher power. Moreover, not only did we achieve the complete recrystallization of the amorphous spot, but also the partial laser-induced recrystallization of Sb_2S_3, which is a promising way to obtain multi-level phase transition in the depth of Sb_2S_3. Therefore, our work paves the way for full control of the all-optical reversible switching of Sb_2S_3 and shows promise for rewritable patterns, encoding information in the depth of PCM and designing dynamically tunable images, holograms and devices.

6. Experimental Section

Sample Fabrication: The Sb_2S_3 and SiO_2 layers were deposited on a silicon substrate by electron beam evaporation at a rate between 0.6 and 1 Å s^{-1} and at an initial pressure around 10^{-6} mbar. The Sb_2S_3 was deposited amorphous and subsequently crystallized thermally for 2 h using a linkam heat cell set at 280°C. The crystallization was realized under ambient pressure. The laser amorphization was performed on the thermally crystallized samples.

Determination of the Amorphization Threshold: To calculate the amorphization threshold, the average power was measured, with a precision of 0.04 mW, at the output of the optical setup where the sample was positioned using a powermeter. Then, the energy was calculated from the laser repetition rate and input it in the Gaussian beam formula. The resulting error on the pulse energy was 1 nJ. The spot diameters were measured under the optical microscope with the microscope software, with a precision of 0.5 µm approximately. The amorphization threshold was the calculated fluence from the Gaussian beam formula for a given energy E and the corresponding spot radius r.

Simulations: The multi-physics simulations were carried out using MATLAB 2023a. The optical stage was a re-implementation of the transfer-method matrix,[38] while the thermal stage was carried out using MATLAB's partial differential equation solver. Given an initial multilayer structure, the optical stage was run first, and the calculated absorbed power density was used as the heat source term in the thermal stage. The thermal simulation was interrupted as soon as 1 nm of crystalline material overshoots the melting point. When this occurs, the multilayer structure was updated to reflect the change in material properties, and both simulation stages were run again. Improper discretization of the problem could be a large source of numerical error, especially due to interfaces where thermal parameters were discontinuous. Hence, a sub-picometric meshing was enforced around all layer interfaces, and the meshing was updated in step with the structure throughout the duration of the simulation.

The main material parameters used are summarized in **Table 2**. The initial and back plate temperatures were both set to 20 °C.

The n and k values were experimental values taken from ellipsometry measurements while the thermal parameters are taken from the literature (Sb_2S_3) or Lumerical database (SiO_2 and Si). The latent heat, representing the energy required to melt the PCM, was assumed to be $\Delta H_f \approx 120$ kJkg^{-1}.[48]

TEM Characterization: Conventional transmission electron microscopy (TEM) observations were performed using a JEOL 2100. The thin foils were prepared from the selected samples via the lift-out method using a Ga LMIS-focused ion beam instrument (Zeiss Crossbeam 550L). The TEM was operated at 200 kV and was equipped with a high-tilt objective lens pole piece. Images were recorded using a bottom-mounted Gatan Orius SC1000 CCD camera with a physical pixel size of 9 × 9 µm. Care was taken to limit the electron dose on the observed foils in order to avoid thermally induced crystallization of the amorphous Sb_2S_3 layer by the electron beam. Bright field and dark field images were obtained by placing a 20 µm aperture near the back focal plane of the objective lens; this corresponds to a collection angle across the aperture disk of 4 mrad. The dark field images were obtained by tilting a diffraction spot of the crystalline Sb_2S_3 onto the optical axis of the microscope. Amorphous parts of the thin foil were visible via mass thickness scattering, which gives a weaker contrast with respect to the diffraction contrast of the c-Sb_2S_3.

Mueller Matrix Characterization: In this work, the microscopic maps of the Block of-diagonal element of the normalized Mueller matrix were recorded with a imaging spectroscopic ellipsometer (Accurion EP4, Park Systems GmBh, Gőttigen Germany) equipped with a 20x objective at a 420 nm wavelength, and an angle of incidence of 50° was reported. The normalized m13 element was displayed, accounting for diattenuation (preferential attenuation of one polarization relative to its orthogonal counterpart) of linearly polarized light along the –45°/+45°. This element was chosen as it evidences best the position-dependant properties of crystalline

Table 2. Material parameters used for the simulations.

	n	k	C_p J.K^{-1}.kg^{-1}	ρ kg.m^{-3}	κ W.K^{-1}.m^{-1}
Sb_2S_3 a	3.55 ± 0.01	0.18 ± 0.03	353[47]	4600[28]	1.16[28]
Sb_2S_3 c	4.72 ± 0.03	0.74 ± 0.04	353[47]	4600[28]	1.16[28]
SiO_2	1.47	0	709	2203	1.38
Si	4.15	0.03	711	2330	148

© 2024 The Author(s). Advanced Optical Materials published by Wiley-VCH GmbH

21951071, 2024, 28, Downloaded from https://advanced.onlinelibrary.wiley.com/doi/10.1002/adom.202401214 by Universidad De Cantabria, Wiley Online Library on [18/02/2025]. See the Terms and Conditions (https://onlinelibrary.wiley.com/terms-and-conditions) on Wiley Online Library for rules of use; OA articles are governed by the applicable Creative Commons License

Sb_2S_3. However, for a complete understanding of the material properties the full Mueller matrix was needed. The latter could be found in the Supporting Information.

Supporting Information

Supporting Information is available from the Wiley Online Library or from the author.

Acknowledgements

The authors acknowledge funding from the French National Research Agency (ANR) under the projects MetaOnDemand (ANR-20-CE24-0013) and OCTANE (ANR-20-CE24-0019). S.V.M. and S.E. acknowledge the project ADONIS (No. CZ.02.1.01/0.0/0.0/ 16-019/0000789) from the European Regional Development Fund. Y.G. acknowledges founding from a Ramon y Cajal Fellowship (RYC2022-037828-I). The authors thank F. Bentata, H. S. Nguyen and X. Letartre for fruitful discussions and D. Troadec for the FIB preparation.

Conflict of Interest

The authors declare no conflict of interest.

Data Availability Statement

The data that support the findings of this study are available from the corresponding author upon reasonable request.

Keywords

laser, nanophotonics, phase-change materials, programmable photonics

Received: May 3, 2024
Revised: June 18, 2024
Published online: August 27, 2024

[1] T. Cui, B. Bai, H.-B. Sun, *Adv. Funct. Mater.* **2019**, *29*, 1806692.
[2] T. Cao, R. Wang, R. E. Simpson, G. Li, *Prog. Quantum Electron.* **2020**, *74*, 100299.
[3] M. Wuttig, H. Bhaskaran, T. Taubner, *Nat. Photonics* **2017**, *11*, 465.
[4] S. Abdollahramezani, O. Hemmatyar, H. Taghinejad, A. Krasnok, Y. Kiarashinejad, M. Zandehshahvar, A. Alù, A. Adibi, *Nanophotonics* **2020**, *9*, 1189.
[5] E. Mikheeva, C. Kyrou, F. Bentata, S. Khadir, S. Cueff, P. Genevet, *ACS photonics* **2022**, *9*, 1458.
[6] C. Ríos, M. Stegmaier, P. Hosseini, D. Wang, T. Scherer, C. D. Wright, H. Bhaskaran, W. H. Pernice, *Nat. Photonics* **2015**, *9*, 725.
[7] F. Brückerhoff-Plückelmann, I. Bente, M. Becker, N. Vollmar, N. Farmakidis, E. Lomonte, F. Lenzini, C. D. Wright, H. Bhaskaran, M. Salinga, B. Risse, W. H. P. Pernice, *Sci. Adv.* **2023**, *9*, eadi9127.
[8] Z. Cheng, C. Ríos, W. H. Pernice, C. D. Wright, H. Bhaskaran, *Sci. Adv.* **2017**, *3*, e1700160.
[9] J. Feldmann, N. Youngblood, C. D. Wright, H. Bhaskaran, W. H. Pernice, *Nature* **2019**, *569*, 208.
[10] M. A. Kats, D. Sharma, J. Lin, P. Genevet, R. Blanchard, Z. Yang, M. M. Qazilbash, D. Basov, S. Ramanathan, F. Capasso, *Appl. Phys. Lett.* **2012**, *101*, 22.
[11] Y. Chen, X. Li, X. Luo, S. A. Maier, M. Hong, *Photon. Res.* **2015**, *3*, 54.
[12] S. Cueff, A. Taute, A. Bourgade, J. Lumeau, S. Monfray, Q. Song, P. Genevet, B. Devif, X. Letartre, L. Berguiga, *Adv. Opt. Mater.* **2021**, *9*, 2001291.
[13] X. Yin, T. Steinle, L. Huang, T. Taubner, M. Wuttig, T. Zentgraf, H. Giessen, *Light: Sci. Appl.* **2017**, *6*, e17016.
[14] C. R. de Galarreta, A. M. Alexeev, Y.-Y. Au, M. Lopez-Garcia, M. Klemm, M. Cryan, J. Bertolotti, C. D. Wright, *Adv. Funct. Mater.* **2018**, *28*, 1704993.
[15] P. Hosseini, C. D. Wright, H. Bhaskaran, *Nature* **2014**, *511*, 206.
[16] D. Wang, L. Zhao, S. Yu, X. Shen, J.-J. Wang, C. Hu, W. Zhou, W. Zhang, *Mater. Today* **2023**.
[17] W. Dong, H. Liu, J. K. Behera, L. Lu, R. J. Ng, K. V. Sreekanth, X. Zhou, J. K. Yang, R. E. Simpson, *Adv. Funct. Mater.* **2019**, *29*, 1806181.
[18] M. Delaney, I. Zeimpekis, D. Lawson, D. W. Hewak, O. L. Muskens, *Adv. Funct. Mater.* **2020**, *30*, 2002447.
[19] A. Biegański, M. Perestjuk, R. Armand, A. Della Torre, C. Laprais, G. Saint-Girons, V. Reboud, J.-M. Hartmann, J.-H. Tortai, A. Moreau, J. Lumeau, T. Nguyen, A. Mitchell, C. Monat, S. Cueff, C. Grillet, *Opt. Mater. Express* **2024**, *14*, 862.
[20] A. Taute, S. Al-Jibouri, C. Laprais, S. Monfray, J. Lumeau, A. Moreau, X. Letartre, N. Baboux, G. Saint-Girons, L. Berguiga, S. Cueff, *Opt. Mater. Express* **2023**, *13*, 3113.
[21] M. Wei, K. Xu, B. Tang, J. Li, Y. Yun, P. Zhang, Y. Wu, K. Bao, K. Lei, Z. Chen, H. Ma, C. Sun, R. Liu, M. Li, L. Li, H. Lin, *Nat. Commun.* **2024**, *15*, 2786.
[22] R. Chen, Z. Fang, C. Perez, F. Miller, K. Kumari, A. Saxena, J. Zheng, S. J. Geiger, K. E. Goodson, A. Majumdar, *Nat. Commun.* **2023**, *14*, 3465.
[23] X. Yang, L. Lu, Y. Li, Y. Wu, Z. Li, J. Chen, L. Zhou, *Adv. Funct. Mater.* **2023**, *33*, 2304601.
[24] D. Lawson, D. W. Hewak, O. L. Muskens, I. Zeimpekis, *J. Opt.* **2022**, *24*, 064013.
[25] T. A. Miller, M. Rudé, V. Pruneri, S. Wall, *Phys. Rev. B* **2016**, *94*, 024301.
[26] X. Sun, M. Ehrhardt, A. Lotnyk, P. Lorenz, E. Thelander, J. W. Gerlach, T. Smausz, U. Decker, B. Rauschenbach, *Sci. Rep.* **2016**, *6*, 28246.
[27] D. Lawson, S. Blundell, M. Ebert, O. L. Muskens, I. Zeimpekis, *Opt. Mater. Express* **2024**, *14*, 22.
[28] H. Liu, W. Dong, H. Wang, L. Lu, Q. Ruan, Y. S. Tan, R. E. Simpson, J. K. Yang, *Sci. Adv.* **2020**, *6*, 51.
[29] Q. Wang, J. Maddock, E. Rogers, T. Roy, C. Craig, K. F. Macdonald, D. Hewak, N. I. Zheludev, *Appl. Phys. Lett.* **2014**, *104*, 12.
[30] P. Li, X. Yang, T. W. Maß, J. Hanss, M. Lewin, A.-K. U. Michel, M. Wuttig, T. Taubner, *Nat. Mater.* **2016**, *15*, 870.
[31] A.-K. U. Michel, P. Zalden, D. N. Chigrin, M. Wuttig, A. M. Lindenberg, T. Taubner, *Acs Photonics* **2014**, *1*, 833.
[32] A. Heßler, S. Wahl, T. Leuteritz, A. Antonopoulos, C. Stergianou, C.-F. Schön, L. Naumann, N. Eicker, M. Lewin, T. W. Maß, M. Wuttig, S. Linden, T. Taubner, *Nat. Commun.* **2021**, *12*, 924.
[33] Q. Wang, E. T. Rogers, B. Gholipour, C.-M. Wang, G. Yuan, J. Teng, N. I. Zheludev, *Nat. Photonics* **2016**, *10*, 60.
[34] K. Gao, F. Qiang, S. Tian, Y. Tan, S. Liu, W. Zhang, T. Mei, *Adv. Opt. Mater.* **2024**, 2302722.
[35] K. Gao, K. Du, S. Tian, H. Wang, L. Zhang, Y. Guo, B. Luo, W. Zhang, T. Mei, *Adv. Funct. Mater.* **2021**, *31*, 35.
[36] X. Sun, A. Lotnyk, M. Ehrhardt, J. W. Gerlach, B. Rauschenbach, *Adv. Opt. Mater.* **2017**, *5*, 1700169.
[37] Y. Zhang, C. Ríos, M. Y. Shalaginov, M. Li, A. Majumdar, T. Gu, J. Hu, *Appl. Phys. Lett.* **2021**, *118*, 21.
[38] T. G. Mackay, A. Lakhtakia, *The Transfer-Matrix Method in Electromagnetics and Optics*, Springer Nature, New York **2022**.
[39] T. Y. Teo, N. Li, L. Y. Tobing, A. S. Tong, D. K. Ng, Z. Ren, C. Lee, L. Y. Lee, R. E. Simpson, *arXiv preprint arXiv:2305.03631* **2023**.

© 2024 The Author(s). Advanced Optical Materials published by Wiley-VCH GmbH

21951071, 2024, 28, Downloaded from https://advanced.onlinelibrary.wiley.com/doi/10.1002/adom.202401214 by Universidad De Cantabria, Wiley Online Library on [18/02/2025]. See the Terms and Conditions (https://onlinelibrary.wiley.com/terms-and-conditions) on Wiley Online Library for rules of use; OA articles are governed by the applicable Creative Commons License

[40] A. Ronchi, P. Homm, M. Menghini, P. Franceschini, F. Maccherozzi, F. Banfi, G. Ferrini, F. Cilento, F. Parmigiani, S. S. Dhesi, M. Fabrizio, J.-P. Locquet, C. Giannetti, *Phys. Rev. B* **2019**, *100*, 075111.
[41] N. Amini, J. Pries, Y. Cheng, C. Persch, M. Wuttig, M. Stolpe, S. Wei, *Mater. Sci. Semicond. Process.* **2021**, *135*, 106094.
[42] M. Schubert, T. Hofmann, C. Herzinger, W. Dollase, *Thin Solid Films* **2004**, *455*, 619.
[43] Y. Gutiérrez, A. Fernández-Pérez, S. A. Rosales, C. Cobianu, M. Gheorghe, M. Modreanu, J. M. Saiz, F. Moreno, M. Losurdo, *Opt. Mater. Express* **2022**, *12*, 1531.
[44] Y. Gutiérrez, A. P. Ovvyan, G. Santos, D. Juan, S. A. Rosales, J. Junquera, P. García-Fernández, S. Dicorato, M. M. Giangregorio, E. Dilonardo, F. Palumbo, M. Modreanu, J. Resl, O. Ishchenko, G. Garry, T. Jonuzi, M. Georghe, C. Cobianu, K. Hingerl, C. Cobet, F. Moreno, W. H. P. Pernice, M. Losurdo, *Iscience* **2022**, *25*, 6.
[45] K. Vilayphone, M. Amara, R. Orobtchouk, F. Mandorlo, S. Mazauric, X. Letartre, S. Cueff, H. S. Nguyen, T. Wood, *ACS Photonics* **2024**.
[46] D. R. Neuville, D. Caurant, L. Cormier, L. Montagne, *Du verre au cristal: Nucléation, croissance et démixtion, de la recherche aux applications*, EDP sciences Les Ulis, France **2013**.
[47] O. Hemmatyar, S. Abdollahramezani, I. Zeimpekis, S. Lepeshov, A. Krasnok, A. I. Khan, K. M. Neilson, C. Teichrib, T. Brown, E. Pop, D. W. Hewak, M. Wuttig, A. Alu, O. L. Muskens, A. Adibi, *arXiv preprint arXiv:2107.12159* **2021**.
[48] G. K. Johnson, G. Papatheodorou, C. E. Johnson, *J. Chem. Thermodyn.* **1981**, *13*, 745.

© 2024 The Author(s). Advanced Optical Materials published by Wiley-VCH GmbH

21951071, 2024, 28, Downloaded from https://advanced.onlinelibrary.wiley.com/doi/10.1002/adom.202401214 by Universidad De Cantabria, Wiley Online Library on [18/02/2025]. See the Terms and Conditions (https://onlinelibrary.wiley.com/terms-and-conditions) on Wiley Online Library for rules of use; OA articles are governed by the applicable Creative Commons License